Aberration-driven tilted emission in degenerate cavities

S. V. Gurevich [1,2,*] F. Maucher [2,3] and J. Javaloyes [2]

[1]*Institute for Theoretical Physics, University of Münster, Wilhelm-Klemm-Str. 9, D-48149 Münster, Germany*
[2]*Departament de Física and IAC³, Universitat de les Illes Balears, C/ Valldemossa km 7.5, 07122 Mallorca, Spain*
[3]*Faculty of Mechanical Engineering, Department of Precision and Microsystems Engineering, Delft University of Technology, 2628 CD, Delft, The Netherlands*

The compensation of chromatic dispersion opened new avenues and extended the level of control upon pattern formation in the *temporal domain*. In this paper, we propose the use of a nearly degenerate laser cavity as a general framework allowing for the exploration of higher contributions to diffraction in the *spatial* domain. Our approach leverages the interplay between optical aberrations and the proximity to the self-imaging condition, which allows us to cancel or reverse paraxial diffraction. As an example, we show how spherical aberrations materialize into a transverse bi-Laplacian operator and, thereby, explain the stabilization of temporal solitons traveling off-axis in an unstable mode-locked broad-area surface-emitting laser. We disclose an analogy between these regimes and the dynamics of a quantum particle in a double-well potential.

I. INTRODUCTION

The understanding of self-organized spatiotemporal patterns is key in photonics and the formation of shocks, vortices, tilted waves, cross-roll patterns, weak optical turbulence, and localized structures was observed experimentally and studied theoretically in large-aspect-ratio lasers, see, e.g., Ref. [1–11]. Another recent example of multidimensional spatiotemporal self-organization is the experimental observation of spatiotemporal mode-locking in multimode optical fibers [12–14].

Dispersion compensation consists in combining elements with opposed chromatic properties to achieve an overall partial or total cancellation of the second-order dispersion. This simple yet powerful idea permitted exploring the influence of higher order contributions. While optical temporal localized structures often result from the balance between self-phase modulation and anomalous second-order dispersion [15–17], it was recently proven that third- and fourth-order dispersion lead to unforeseen effects such as the stabilization of solitons and frequency combs [18–20], symmetry breaking [21], the control of modulational instabilities [22,23], or the realization of purely quartic solitons [24,25] as predicted in Ref. [26].

The paraxial diffraction emerging as a beam propagate is mathematically equivalent to that of second-order chromatic dispersion. Optical cavities in which the path of light is folded onto itself may contain a transverse plane that is its own image after a round trip [27,28]. This so-called stigmatic condition is equivalent to an effective cancellation of

paraxial diffraction. Additionally imposing the nullification of the round-trip wavefront curvature does not only achieve the self-imaging condition (SIC) for the field intensity but also for its *amplitude*. Self-imaging cavities have attracted a great deal of attention for their rich spatiotemporal dynamics [5,10,29–32] and for their application in speckle-free imaging [33,34], frequency comb multiplexing [35], and controllable and reconfigurable multimode fields [36,37]; see Ref. [38] for a review. The proximity of the SIC was used to manipulate the spatial coherence of the field [34,36,39–41], create a perfect coherent absorber [42], realizing topological band structures [43], or to form propagation invariant beams [44]. Aberrations become crucial as the SIC is approached [31,45,46], yet, their effect on spatiotemporal laser dynamics received comparatively less attention. Photonic crystals also allow for dispersion control [47,48] and lead to the zero-diffraction regime [49]. Higher order spatial operators occur in fiber lasers [50] and in optical cavities either at the onset of bistability [51] or containing a photorefractive or semiconductor medium [2–4,52]. Diffraction control was also proposed using metamaterials [53–56] or atomic resonances [57].

In this paper, we study theoretically how aberrations appear as leading effects in nearly degenerate broad-area surface-emitting lasers. We show that these effects can crucially modify the spatiotemporal mode-locking dynamics and give rise to either spatially tilted beams or off-axis temporal solitons. Our results represent a step further towards a more comprehensive understanding of spatiotemporal mode-locking [12–14], the realization of fully confined three-dimensional light bullets [10,58,59], and may lead to new ideas and applications for beam steering, tweezing [60], and tailored optical energy potential landscapes [61,62].

II. TILTED HERMITE-GAUSS MODES

The dynamics of the transverse profile of the field close to the SIC and in the presence of spherical aberrations is

---

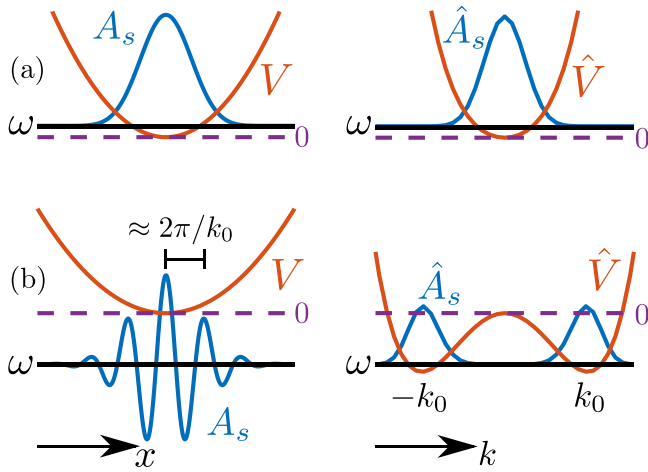*Corresponding author: gurevics@uni-muenster.de

FIG. 1. Schematic of the fundamental Hermite-Gauss (HG) mode $A_s(x)$ (blue) and the corresponding potential $V(x)$ (orange) of Eq. (1) in the real (left) and Fourier space (right) for (a) $b < 0$, $c > 0$ and $s = 1$ (b) $b > 0$, $c > 0$, and $s = 1$. The resulting double-well potential in the Fourier space with the minima located at k_0 shown in (b) corresponds to a tilted HG mode in the real space.

equivalent to the dynamics of a quantum harmonic oscillator featuring a fourth-order derivative

$$-i\partial_\theta A = \left(cx^2 + b\partial_x^2 + s\partial_x^4\right)A, \qquad (1)$$

where c, b, and s are real coefficients that correspond to the residual wavefront curvature, diffraction, and spherical aberrations, respectively. We will focus our attention on spherical aberrations, as it is often the dominant form of aberration. A detailed derivation of Eq. (1) is provided in the Appendix. Note that Eq. (1) was studied already, albeit in a different context, in Ref. [63].

It is well-known that the potential $V(x) = c\,x^2$ in Eq. (1) supports localized solutions for $bc < 0$ [28]. Setting $A(x, \theta) = A_s(x)e^{-i\omega\theta}$, with ω denoting the frequency of the eigenmode and imposing boundedness of the solution, defines a singular Sturm-Liouville problem (SLP) that allows determining ω:

$$\left(\omega + cx^2 + b\partial_x^2 + s\partial_x^4\right)A_s = 0, \quad \lim_{x\to\pm\infty} A_s = 0. \qquad (2)$$

For $bc < 0$ and $s = 0$, the solutions of Eq. (2) are the so-called Hermite-Gauss (HG) modes $H_n(\frac{x}{\sigma})$ with $\sigma^2 = \sqrt{(-b/c)}$ and frequencies $\omega_n = \frac{b}{\sigma^2}(2n + 1)$ while $n \in \mathbb{N}$ is the modal index. We will see later that this situation corresponds to the case of a stable cavity devoid of aberration.

The HG modes are invariant under Fourier transform since the multiplicative and differential terms in Eq. (1) are exchanged upon performing the latter. However, the role played by the fourth-order derivative in Eq. (1) becomes more clear in Fourier space, where the SLP becomes

$$\left(\omega + c\partial_k^2 - bk^2 + sk^4\right)\hat{A}_s = 0. \qquad (3)$$

Here, we defined $\hat{A}_s$ as the Fourier transform of A_s. Hence, the presence of a fourth-order derivative in Eq. (1) converts the situation to that of a particle in a single- or double-well potential. In case of $b < 0$ and $c > 0$, the potentials $V(x)$ and $\hat{V}(k) = -b\,k^2 + sk^4$ both feature a minimum at the origin as shown in Fig. 1(a).
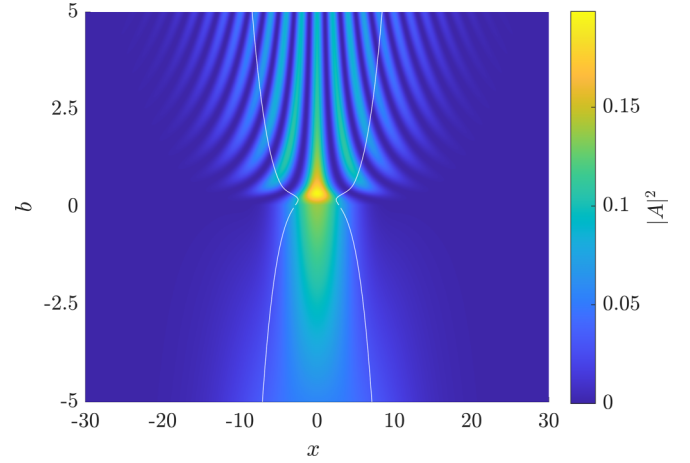

FIG. 2. Numerical solution of Eq. (1) for different values of b and fixed values of $s = 1$ and $c = 4.97 \times 10^{-4}$. White lines indicate the values of $\pm\sqrt{\langle x^2|A|^2\rangle}$.

The bounded solutions of Eq. (1) remain practically unaffected by small values of s, since the solutions remain concentrated at low values of k for which $bk^2 \gg sk^4$. Let us now consider the situation where b changes its sign, which usually signals the transition from a stable to an unstable cavity. In that case, the potential $\hat{V}(k)$ develops a negative curvature around $k = 0$ for $b > 0$. If there were no aberrations present in the system, i.e., $s = 0$, the laser would simply turn off as there is no transverse mode to support emission. Mathematically speaking, this means that the bounded solutions of the SLP cease to exists.

However, the situation can be remedied by the fourth-order derivative as depicted in Fig. 1(b): For $s > 0$, two new minima emerge symmetrically at $k_0 = \pm\sqrt{b/2s}$, which allows bounded solutions to continue to exist in the otherwise unstable domain. The ground-state solution $\hat{A}_s(k)$ in Fourier space can be approximated by a superposition of two bell-shaped functions localized around $\pm k_0$ which, in real space, amounts to a strongly modulated eigenmode with wavelength $\lambda_\perp = 2\pi/k_0$, akin to the interference between Bose-Einstein condensates in a double-well potential [64,65]. This situation is depicted in Fig. 2, where we solved for the ground state of Eq. (1) numerically using complex time evolution. Note that the waist of the mode decreases monotonically upon approaching $b = 0$, but remains finite at $b = 0$. This is due to the fact that the higher order derivative start to play a more dominant role. In the unstable range $b > 0$, we notice that the second-order moment increases, albeit at a faster rate. While we could not obtain closed form analytical solutions of Eq. (2) for $s \neq 0$, the following change of variable

$$A(x) = A_s(x)\exp\left[ik_0 x - \omega\theta\right], \quad k_0 = \sqrt{\frac{b}{2s}}, \qquad (4)$$

permits canceling the first-order derivative and leads to

$$\left(\omega - \frac{b^2}{4s} + cx^2 - 2b\partial_x^2 + i\sqrt{8bs}\partial_x^3 + s\partial_x^4\right)A_s = 0. \qquad (5)$$

Slowly varying envelope solutions, where the characteristic length scale for the envelope A_s is much larger than $2\pi/k_0$ correspond to the inequality $|\partial_x A_s| \ll |k_0 A_s|$. If this condition
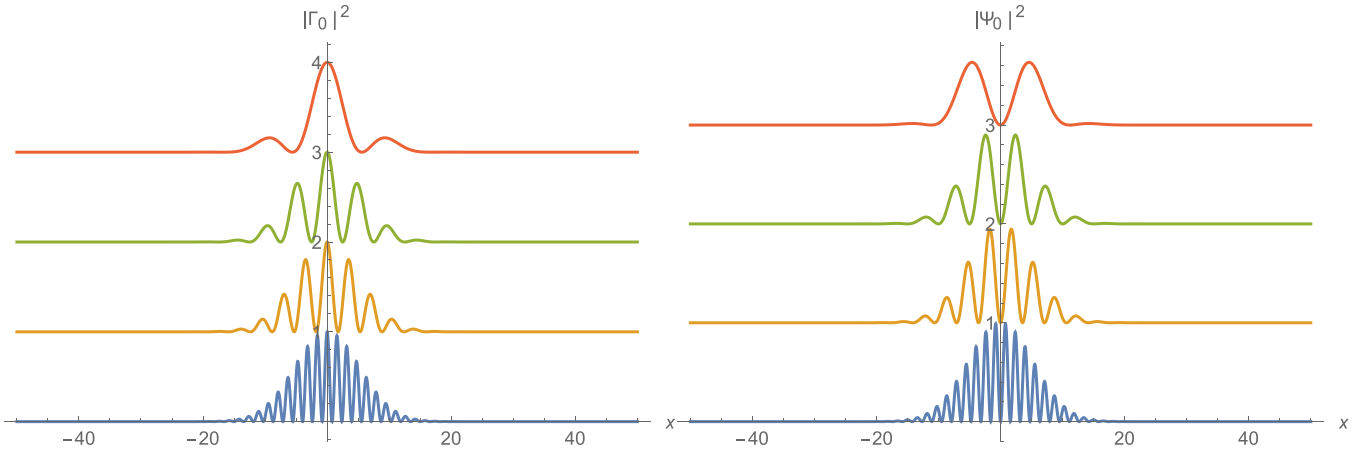
FIG. 3. Evolution of $|\Gamma_0(x,0)|^2$ and $|\Psi_0(x,0)|^2$ as a function of s. Traces are shifted for clarity. From top to bottom, $s = (5, 1, 0.5, 0.1)$. Other parameters are $(b, c) = (0.7873, 0.0004973)$.

is fulfilled, one may neglect the third- and fourth-order derivatives in Eq. (5), leading to

$$\left(\omega - \frac{b^2}{4s} + cx^2 - 2b\partial_x^2\right)A_s = 0. \quad (6)$$

By comparing Eq. (1) with Eq. (2) we note that the latter is again a HG equation where the parameter b has been replaced by $-2b$, which fully explains the increased diverging rate of the second moment in Fig. 2. We note that the frequencies ω are shifted due to the additional term $b^2/(4s)$.

In summary, we disclose the surprising result that an unstable cavity does not necessarily turn off upon crossing the SIC, and lasing eigenmodes can still be supported by spherical aberrations. The modes can be approximated by

$$A(x,\theta) = H_n\left(\frac{x}{\sigma}\right)\exp\left[i(k_0 x - \omega_n \theta)\right], \quad (7)$$

$$\omega_n = \frac{b^2}{4s} - \frac{2b}{\sigma^2}(2n+1), \quad (8)$$

$$\sigma^2 = \sqrt{\frac{2b}{c}}, \quad k_0 = \sqrt{\frac{b}{2s}}. \quad (9)$$

Since $k_0 \in \mathbb{R}$, it is convenient to define two families of eigenfunctions $\Gamma_n(x,\theta)$ and $\Psi_n(x,\theta)$ as

$$\Gamma_n(x,\theta) = H_n\left(\frac{x}{\sigma}\right)\cos(k_0 x)e^{-i\omega_n\theta}, \quad (10)$$

$$\Psi_n(x,\theta) = H_n\left(\frac{x}{\sigma}\right)\sin(k_0 x)e^{-i\omega_n\theta}. \quad (11)$$

The latter are depicted in Figs. 3 and 4, respectively. We observe the effect of the parameter s on the ground states Γ_0 and Ψ_0 in Fig. 3. To stabilize a bounded eigenmode, the decrease of s must be compensated by additional oscillations and, therefore, an increase in $k_0 \sim 1/\sqrt{s}$. In Fig. 4, we also depict how the intensity of the modes $\Gamma_n(x,\theta)$ and $\Psi_n(x,\theta)$ alternate between even and odd when varying n.

We now turn our attention to the two-dimensional (2D) transverse profile whose evolution is governed by

$$-i\frac{\partial A}{\partial \theta} = \left(c_x x^2 + c_y y^2 + b_x \partial_x^2 + b_y \partial_y^2 + s\nabla_\perp^4\right)A. \quad (12)$$

Here, we assume that the tilt cavity possesses two orthogonal axes denoted $\boldsymbol{r}_\perp = (x,y)$ and, for the sake of generality, we

introduced dichroism in Eq. (12), i.e., $b_x \neq b_y$ and $c_x \neq c_y$. The effect of spherical aberration in 2D translates into a bi-Laplacian operator $\nabla_\perp^4 = \partial_x^4 + 2\partial_x^2\partial_y^2 + \partial_y^4$. We note that $\nabla_\perp^4$ is the only fourth-order operator that preserves the rotational symmetry both in real and in Fourier space, which is consistent with the idea of spherical aberration. The equivalent SLP for $A(\boldsymbol{r}_\perp,\theta) = A_s(\boldsymbol{r}_\perp)\exp(-i\omega\theta)$ reads

$$0 = \left(\omega + c_x x^2 + c_y y^2 + b_x \partial_x^2 + b_y \partial_y^2 + s\nabla_\perp^4\right)A_s. \quad (13)$$

When $s = 0$ and the two conditions $b_x c_x < 0$ and $b_y c_y < 0$ are simultaneously verified, the SLP admits separable solutions that are simply the product of the HG modes in the x and y directions discussed previously [28]. We now consider the effect of aberration close to the SIC when the cavity becomes unstable. Due to the inherent dichroism present in any realistic experimental system, one can assume that the cavity becomes unstable first in one direction, say the x direction. Applying the Fourier transform to Eq. (13) leads to

$$0 = \left[\omega + c_x \partial_{k_x}^2 + c_y \partial_{k_y}^2 + \hat{V}(\boldsymbol{k}_\perp)\right]A_s, \quad (14)$$

where we defined the potential in Fourier space:

$$\hat{V}(\boldsymbol{k}_\perp) = -b_x k_x^2 - b_y k_y^2 + s\left(k_x^2 + k_y^2\right)^2. \quad (15)$$

A representation of $\hat{V}(\boldsymbol{k}_\perp)$ for three different values of b_x is given in Fig. 5. We see that the transition from a stable to an unstable cavity is obtained when b_x changes its sign from negative to positive, which gives rise to the appearance of two new minima as observed in the 1D case in Fig. 1. Their position is obtained by simply setting $\partial_{k_x}\hat{V} = \partial_{k_y}\hat{V} = 0$, which leads to $\boldsymbol{k}_\perp^\pm = \pm(\sqrt{\frac{b_x}{2s}}, 0)$. As already discussed, this corresponds to off-axis emission on the x axis and stable on-axis emission on the y axis. The curvature of $\hat{V}(\boldsymbol{k}_\perp)$ around the two minima in $\boldsymbol{k}_\perp^\pm$ upon back-transforming to direct space corresponds to the effective diffraction experienced by a wave-packet centered around this tilted wave vector $\boldsymbol{k}_\perp^\pm$. We obtain

$$\frac{1}{2}\frac{\partial^2 \hat{V}}{\partial k_x^2} = 2b_x, \quad \frac{1}{2}\frac{\partial^2 \hat{V}}{\partial k_y^2} = b_x - b_y, \quad \frac{\partial^2 \hat{V}}{\partial k_x \partial k_y} = 0. \quad (16)$$

The curvature in the x direction changed from $-b_x \rightarrow 2b_x$, similarly to the 1D case. However, the perpendicular direction
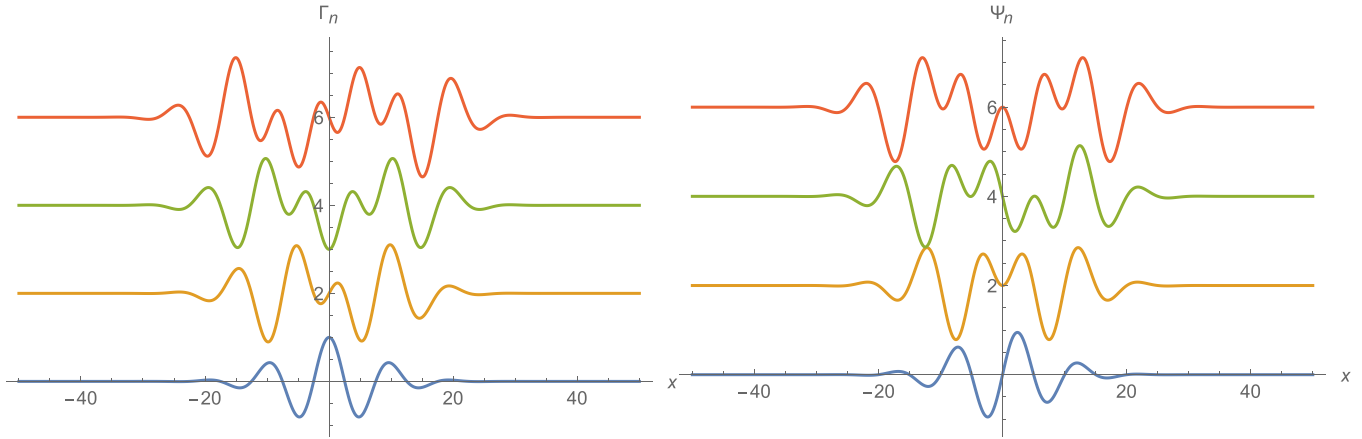
FIG. 4. Evolution of $\Gamma_n(x, 0)$ and $\Psi_n(x, 0)$ as a function of the modal index n. We note the even/odd alternating sequence. Traces are shifted for clarity. From top to bottom, $n = (3, 2, 1, 0)$. Other parameters are $(b, c, s) = (0.7873, 0.0004973, 1)$.

is also affected by the off-axis emission, leading to the substitution $b_y \rightarrow b_y - b_x$. In the case of a cavity that changes behavior from stable $b_x < 0$ to unstable $b_x > 0$, the off-axis emission along the x direction that restabilizes the emission renders the perpendicular direction more diffractive since $b_y - b_x < b_y$ if $b_x > 0$. The results of Fig. 5 entice us to seek again a modulated profile

$$A(\boldsymbol{r}_\perp) = A_s(\boldsymbol{r}_\perp) \exp\left[i(k_0 x - \omega\theta)\right] \quad (17)$$

with $k_0 = \sqrt{b_x/(2s)}$. Truncating to second order, we get the approximate SLP problem

$$\frac{b_x^2}{4s} - \omega = \left[c_x x^2 + c_y y^2 - 2b_x \partial_x^2 + (b_y - b_x)\partial_y^2\right]A_s, \quad (18)$$

where the modification of the diffraction coefficients in Eq. (18) is fully consistent with the discussion of the curvature of $\hat{V}$ given in Eq. (16). The eigenmodes of such an unstable cavity are the product of a modulated HG mode in the unstable direction and a regular HG mode in the y direction. As such, we define the eigenmode family with two modal indices (n, m):

$$\Gamma_{n,m}(\boldsymbol{r}_\perp, \theta) = H_n\left(\frac{x}{\sigma_x}\right) H_m\left(\frac{y}{\sigma_y}\right) \cos(k_0 x) e^{-i\omega_{n,m}\theta},$$

$$\Psi_{n,m}(\boldsymbol{r}_\perp, \theta) = H_n\left(\frac{x}{\sigma_x}\right) H_m\left(\frac{y}{\sigma_y}\right) \sin(k_0 x) e^{-i\omega_{n,m}\theta},$$

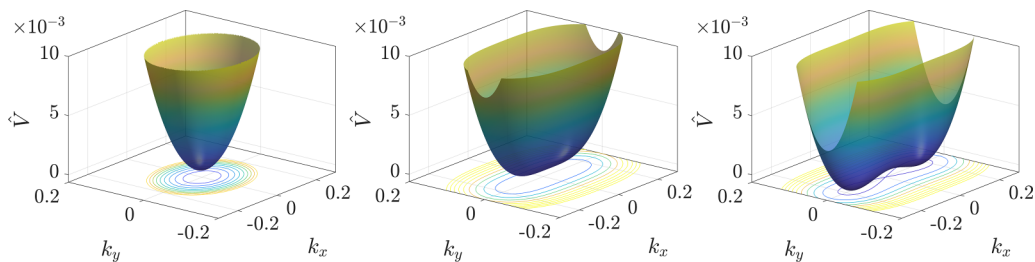$$\omega_{n,m} = \frac{b_x^2}{4s} - \frac{2b_x}{\sigma_x^2}(2n+1) + \frac{b_y - b_x}{\sigma_y^2}(2m+1),$$

$$\sigma_x^2 = \sqrt{2b_x/c_x},$$
$$\sigma_y^2 = \sqrt{(b_x - b_y)/c_y}. \quad (19)$$

III. MULTIDIMENSIONAL MODE-LOCKED TILTED PATTERNS

The situation considered in Eq. (1) materializes, for instance, in the study of passively mode-locked integrated external-cavity surface-emitting laser (MIXSELs) in a near-degenerate cavity [29] as depicted in Fig. 6. Here, the gain (G) and saturable absorber (SA) media are enclosed in a single microcavity and the external mirror is assumed to be ideal while the collimating lens is not. Our modeling approach is based on a Haus master equation model for passive mode-locking (PML) adapted to the experimentally relevant long cavity regime [59,66–68], where the PML pulses become individually addressable temporal localized states (TLSs). The Haus equation relates the slow evolution of the three-dimensional intracavity field $E(\boldsymbol{r}_\perp, t, \theta)$ to the dynamics of the population inversion in the gain $N_1(\boldsymbol{r}_\perp, t)$ and the saturable absorber $N_2(\boldsymbol{r}_\perp, t)$ as

$$\frac{\partial E}{\partial \theta} = [(1 - i\alpha_1)N_1 + (1 - i\alpha_2)N_2 - \kappa + \mathcal{L}]E, \quad (20)$$

$$\frac{\partial N_1}{\partial t} = \gamma_1(J_1 - N_1) - N_1|E|^2, \quad N_1(\boldsymbol{r}_\perp, 0) = J_1, \quad (21)$$

$$\frac{\partial N_2}{\partial t} = \gamma_2(J_2 - N_2) - \hat{s}N_2|E|^2, \quad N_2(\boldsymbol{r}_\perp, 0) = J_2. \quad (22)$$

FIG. 5. Birth of two symmetrically located minima for the Fourier potential $\hat{V}$ for a stable, marginal, and unstable cavity with (from left to right) $b_x = (-0.2, 0, 0.05)$. Other parameters are $(b_y, s) = (-0.8, 1)$.
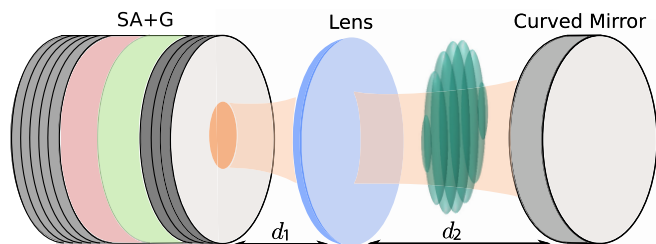
FIG. 6. A schematic of the MIXSEL, where both the gain (green) and the saturable absorption (pink) are contained in the same microcavity. It is coupled face to face to a distant external mirror by an imperfect self-imaging system.

In this formalism, the variable $t \in [0, \tau]$ represents the round-trip time in the external cavity and θ is a second dimensionless time scale normalized by τ. The latter corresponds to the slow evolution of the pulse under the combined effect of gain, absorption and spatiotemporal filtering. The two transverse dimensions are denoted $\mathbf{r}_\perp = (x, y)$ and allow for pattern formation in the plane perpendicular to the propagation direction of the pulse, cf. Fig. 6. Note that in the long cavity regime, the spatiotemporal distributions of the carriers $N_j(\mathbf{r}_\perp, t)$ are slaved to the evolution of the optical field [66,68] and do not depend explicitly on the slow timescale θ. In this regime, one can safely assume a full recovery of the carrier between pulses and a total loss of memory from one round trip toward the next one. In Eqs. (20)–(22), we define κ as the round-trip cavity losses and α_j are the linewidth enhancement factors of the two active media that relax with timescales γ_j^{-1} toward the equilibrium values J_j. The ratio of the saturation fluence of the gain and of the SA is denoted by $\hat{s}$. A standard pseudospectral split-step method was used for the numerical simulations [59]. The effective cavity spatiotemporal linear operator $\mathcal{L}$ accounts for the finite gain bandwidth and chromatic dispersion but also for nonperfect imaging conditions, diffraction, parabolic wavefront curvature, and mirror losses due to finite aperture. $\mathcal{L}$ is given by

$$\mathcal{L} = d_g \partial_t^2 + \mathcal{L}_\perp, \tag{23}$$

where d_g is the temporal diffusion coefficient representing the gain bandwidth and $\mathcal{L}_\perp$ is a transverse round-trip operator.

The Fresnel transform [69] permits calculating the transverse effects occurring at each round trip analytically from the round-trip (ABCD) matrix in the paraxial approximation [28]. In the presence of aberrations, its calculation is achieved by expanding the exact (nonparaxial) operator corresponding to the lens as a sum of an ideal element plus a deviation. The latter potentially contains all the wavefront curvature contributions beyond the parabolic approximation. Assuming a large ratio between the focal length of the mirror and that of the lens permits expressing the spherical aberrations as a bi-Lapacian operator, see the Appendix for details. The transverse round-trip operator $\mathcal{L}_\perp$ in one transverse dimension is given by

$$\mathcal{L}_\perp = icx^2 + (d_f + ib)\partial_x^2 + is\partial_x^4. \tag{24}$$

The finite size of lenses and the numerical aperture of the whole optical system is modeled by a soft aperture and a real

transverse diffusion parameter d_f. Finally, b is the normalized paraxial diffraction parameter and c is the normalized parabolic wavefront curvature. The latter are the off-diagonal elements of the round-trip ABCD matrix [28], and s is the spherical aberration parameter. We note that moving the MIXSEL chip in Fig. 6 modifies b while moving the mirror modifies both b and c.

A qualitative model for the transverse profile of the TLSs such as the one derived in Refs. [10,59] can be obtained by essentially adapting New's method for PML [70] to the situation at hand. This method exploits the scale separation occurring between the pulse evolution, the so-called fast stage in which stimulated emission is dominant, and the slow stage that is controlled by the gain recovery processes. Assuming, as in Refs. [10,59], that the spatiotemporal profile $E(\mathbf{r}_\perp, t, \theta)$ can be factored as $E(\mathbf{r}_\perp, t, \theta) = A(\mathbf{r}_\perp, \theta)p(t)$, with $p(t)$ a normalized TLS profile, one obtains a Rosanov equation [71] for the slow evolution of the TLS transverse profile $A(\mathbf{r}_\perp, \theta)$ as

$$\partial_\theta A = [f(|A|^2) + \mathcal{L}_\perp]A. \tag{25}$$

We define the effective nonlinearity as

$$f(P) = (1 - i\alpha_1)J_1\, g(P) + (1 - i\alpha_2)J_2\, g(\hat{s}P) - \kappa. \tag{26}$$

The nonlinear response of the active material to a pulse is given by $g(P) = (1 - e^{-P})/P$ [10,59,70].

Equations (25) and (26) provide a unified framework which allows bridging our results for spatiotemporal dynamics with the former results of Refs. [71,72] for the case of static autosolitons in bistable interferometers. There, the function $g(P)$ should be replaced by the saturated line-shape transition $\sim (1 + P)^{-1}$. As such, our discussion of the effect of aberrations close to SIC is equally valid for temporal solitons, regular mode-locking, and CW beams such as the tilted beam solutions observed in [29,32].

In one-dimension, Eq. (1) is recovered for the empty cavity, i.e., $f = 0$. Hence, we expect the emergence of a *stable* family of Γ_n and Ψ_n tilted HG modes (10,11) in the *unstable cavity*, where the condition $bc < 0$ is violated. We performed a bifurcation analysis of Eq. (25) in one transverse dimension using path-continuation framework pde2path [73]. The results are summarized in Fig. 7 in the unstable cavity regime, where the peak powers for the fundamental tilted modes Γ_0 (red) and Ψ_0 (blue) are shown in Fig. 7(a) as a function of the gain bias J_1 normalized to the threshold value J_{th}. Furthermore, two exemplary profiles of Γ_0 and Ψ_0 at the same fixed gain value (gray dashed line) are depicted in Figs. 7(b) and 7(c), respectively. For both modes, we observe the typical subcritical transition that leads to bistable TLSs as detailed in Refs. [17,59]. The high intensity branch is stable while the lower branch is unstable and creates a separatrix with the stable off solution. For the parameters chosen, the leftmost limiting fold bifurcations F_1 and F_2 are almost identical for Γ_0 and Ψ_0. A small region of the Andronov-Hopf (AH) instability for Γ_0 exists between points H_{22} and H_{23}. In this region, a small amplitude oscillation is visible in time simulations. Both modes are limited by the AH bifurcations H_{11} and H_{24}, respectively, for high gain values. We stress that these nonlinear modulated HG modes that are solutions of Eqs. (25) and (26) correspond to a train of TLSs whose profile is a tilted beam supported by spherical aberrations in an unstable cavity.
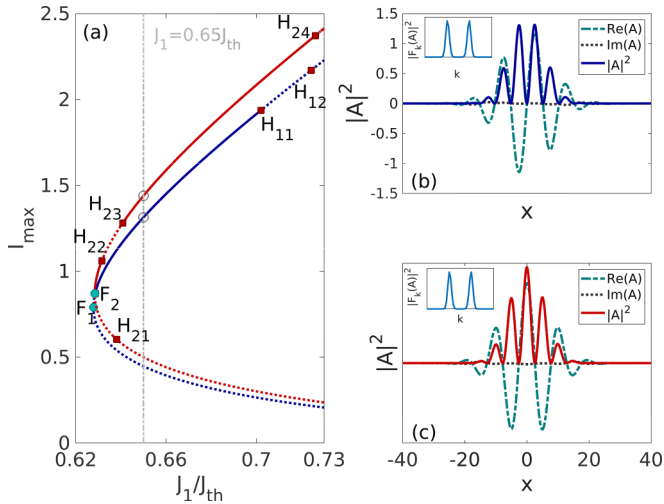
FIG. 7. (a) Branches of one-dimensional tilted HG modes Γ_0 (red) and Ψ_0 (blue) of Eq. (25) as a function of the normalized gain bias J_1/J_{th}. The mode Γ_0 is stable (solid line) between the fold F_2 (cyan circle) and the AH point H_{22} as well as between AH points H_{23} and H_{24} (red squares), respectively. The mode Ψ_0 gains the stability at the fold F_1 and remains stable up to the AH bifurcation point H_{11}. (b), (c) Exemplary profiles of Γ_0 and Ψ_0 for $J_1 = 0.65J_{th}$ (gray dashed line). Real (turquoise, dashed), imaginary (black, dotted), and intensity fields (blue, red, solid), respectively, are presented. Parameters are $\alpha_1 = 1.5$, $\alpha_2 = 0.5$, $J_2 = -0.06$, $\hat{s} = 15$, $\kappa = 0.035$, $d_f = 10^{-4}$, $b = 0.78$, $c = 4.97 \times 10^{-4}$, $s = 1.0$.

In two spatial dimensions, we assume the system to be weakly astigmatic and, as discussed previously, that the SIC is not reached simultaneously for both transverse dimensions. For a cavity that is stable in the vertical and unstable in the horizontal direction, we observed the tilted localized patterns

shown in Figs. 8(a)–8(c) by solving Eqs. (25) and (26) numerically. The typical evolution for large values of b_x (i.e., entering more deeply into the unstable region) is presented together with the corresponding far-field power spectrum $|\hat{A}|^2$. Figures 8(d)–8(f) show the two peaks in the far field related to the value of the transverse horizontal wave-number $\pm k_0$. Clearly, an increase of b_x leads to an increase of k_0, which corresponds to a higher frequency of the mode oscillations in the near field. These results would correspond closely to the experimental situation described either in Ref. [29,74] for a mode-locked vertical surface-emitting external-cavity semiconductor laser using a saturable absorber or in Ref. [32] for a CW broad area laser. Our analysis uses a bi-Laplacian operator that approximates the effect of spherical aberrations. However, we verified that a more rigorous treatment using the Fox-Li method yielded similar results for the modal structure of the unstable cavity.

IV. CONCLUSIONS

In conclusion, we have investigated the effect of wavefront aberrations in a degenerated cavity. We found that the interplay between spherical aberrations and the proximity to the SIC may lead to modulated beams that can support either CW or temporal solitons in a mode-locked broad-area MIXSEL. These modulated beams are analogous to the eigenmodes of a quantum particle in a double-well potential. They can be analytically approximated by spatially modulated HG modes. We linked the wavelength of their modulation to the parameters of the cavity. We note that the transition from a stable towards an unstable cavity around SIC can be obtained in two ways: Either for $c > 0$ and changing the sign of b from negative to positive or for $c < 0$ and changing the sign of b correspondingly. These two situations are not identical with
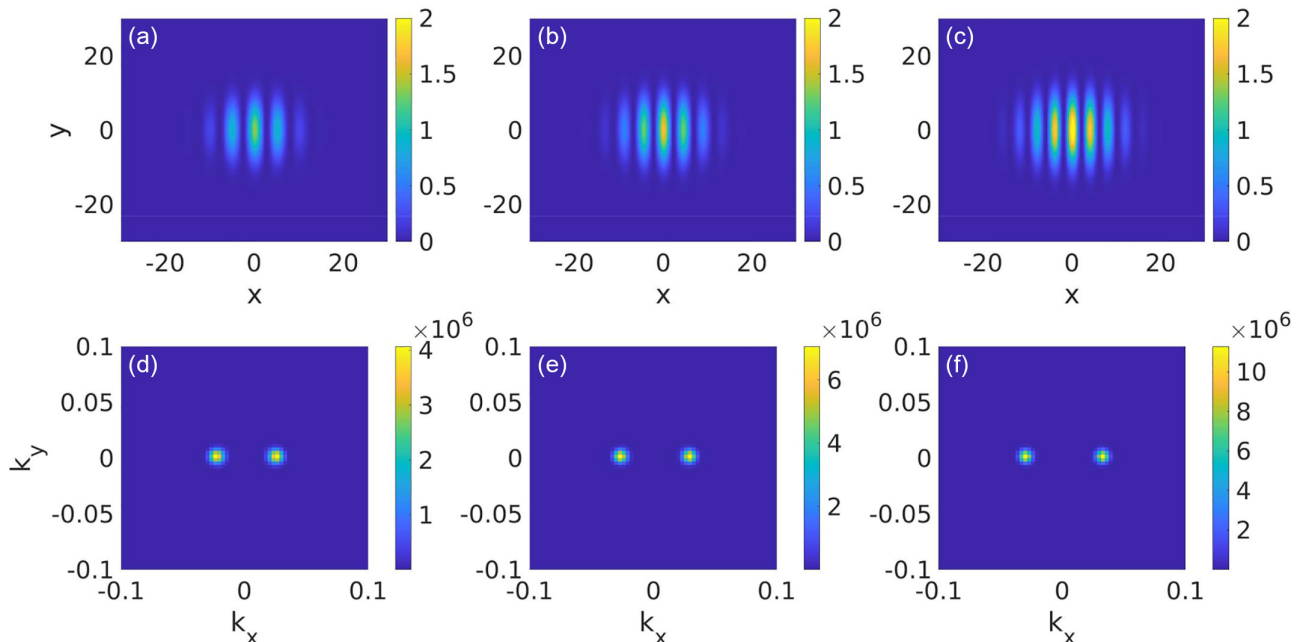

FIG. 8. (a)–(c): Intensity profiles of the 2D pattern obtained by the numerical simulations for three values of $b_x = (0.78, 1.02, 1.25)$, respectively, at the fixed value of the current $J_1 = 0.65J_{th}$. (d)–(f) Corresponding power spectra in the (k_x, k_y) plane. Parameters are $b_y = -0.39$, $c_x = c_y = 4.97 \cdot 10^{-4}$. Other parameters as in Fig. 7.

respect to the effect of spherical aberrations since the off-axis wave vector $k_0 = \sqrt{b/2s}$ requires b and s to have the same sign. As such, the sign of s dictates the situation in which one can observe these modulated HG beams. While we focused on the influence of spherical aberrations, we proposed a general framework that, in principle, permits calculating the effect of the other Seidel aberrations such as coma, distortion, or field curvature in a cavity close to SIC. We believe that exhibiting the link between these wavefront curvature defects and their equivalent representations as spatial operators provides a framework that could lead to a range of interesting research avenues in photonics. Furthermore, the condition of a large ratio between the focal distances of the aberrated lens and the nonaberrated other elements could be relaxed. In this situation, spherical aberrations translate into nonlocal spatial operators that may lead to rich pattern formation scenarios, as observed in other fields [75–77].

APPENDIX: SPHERICAL ABERRATION CLOSE TO THE SIC

In this Appendix, we derive how the effect of spherical aberrations can be recast into the form of a bi-Lapacian differential operator in the paraxial equation governing the field evolution after each round trip. We will use the formalism of wave optics provided by generalized Huygens–Fresnel transform (HFT) for ABCD systems [28]. We note that the HFT allows for the composition of parabolic operators, i.e., quadratic wavefront profiles induced by parabolic lenses as well as paraxial diffraction, since the latter also corresponds to a parabolic operator in Fourier space. We characterize our system by an *ABCD* round-trip matrix

$$W = \begin{pmatrix} A & B \\ C & D \end{pmatrix}, \quad (A1)$$

with $\det(W) = AD - BC = 1$. The generalized HFT for the passage of light through a first-order optical system [69] composed of parabolic elements is given in one transverse dimension by

$$O(x, l) = \sqrt{\frac{-i}{\lambda B}} e^{ikl} \int_{-\infty}^{\infty} O(\xi, 0)$$
$$\times \exp\left[i\frac{\pi}{\lambda B}(A\xi^2 - 2x\xi + Dx^2)\right] d\xi, \quad (A2)$$

where $O(x, 0)$ is the incoming field passing through the system characterized by the *ABCD* matrix W and $k = 2\pi/\lambda$ is the wave vector of light. We note that B plays the role of a propagation distance while C is an inverse of a dis-

tance and represents wavefront curvature. Further, A, D are dimensionless quantities that correspond to spatial and angular magnification, respectively.

Close to the SIC, we consider the limit $B \to 0$ which renders Eq. (A2) singular. This difficulty can be avoided by factoring the quadratic form as follows:

$$A\xi^2 - 2x\xi + Dx^2 = A\left(\xi - \frac{x}{A}\right)^2 + \left(D - \frac{1}{A}\right)x^2. \quad (A3)$$

Using that $(D - \frac{1}{A})/B = C/A$, the Huygens-Fresnel integral given in Eq. (A2) becomes

$$O(x, l) = e^{ikl} e^{i\frac{\pi}{\lambda}\frac{C}{A}x^2} \int_{-\infty}^{\infty} O(\xi, 0)$$
$$\times \sqrt{\frac{-i}{\lambda B}} \exp\left[i\frac{\pi A}{\lambda B}\left(\xi - \frac{x}{A}\right)^2\right] d\xi. \quad (A4)$$

Equation (A4) will be the form of the Huygens–Fresnel integral used in the rest of the Appendix.

As mentioned in the main text, we consider the simplest case of the self-imaging cavity [29] consisting of one lens of focal length f and one mirror or radius of curvature R, separated by distances d_1 and d_2, see Fig. 6. The resulting round-trip propagation matrix reads

$$W = D_1 L_0 D_2 M D_2 L_0 D_1, \quad (A5)$$

with

$$D_j = \begin{pmatrix} 1 & d_j \\ 0 & 1 \end{pmatrix}, \quad (A6)$$

$$L_0 = \begin{pmatrix} 1 & 0 \\ -\frac{1}{f_0} & 1 \end{pmatrix}, \quad (A7)$$

$$M = \begin{pmatrix} 1 & 0 \\ -\frac{2}{R} & 1 \end{pmatrix}. \quad (A8)$$

The SIC for which one finds $W = \mathrm{Id}$ is encountered for the following values of of $d_{1,2}$:

$$d_1^* = f + \frac{f^2}{R}, \quad (A9)$$

$$d_2^* = f + R. \quad (A10)$$

Expanding to first order in $\delta d_j = d_j - d_j^*$, one obtains

$$T = \begin{pmatrix} 1 & 2\left(\delta d_1 + \delta d_2 \frac{f^2}{R^2}\right) \\ -\frac{2}{f^2}\delta d_2 & 1 \end{pmatrix}. \quad (A11)$$

We conclude that, close to the SIC, small displacements from the MIXSEL chip induce a B coefficient, whereas moving the mirror modifies both the values of B and C. Finally, we can safely assume that $A = D = 1$ at first order in $\mathcal{O}(\delta d_j)$. In addition to small deviations from the SIC, we consider that the focal length of the lens depends on its radial position and we model the spherical aberration as $f(x) = f_0 + \sigma x^2$. Denoting the field profile before and after the lens as E_i and E_o, respectively, we have

$$E_o(x) = e^{-i\frac{\pi}{\lambda}\frac{x^2}{f}} E_i(x). \quad (A12)$$

Denoting the operator corresponding to the effect of the lens by L, we separate the contribution from the unperturbed lens

with focal length f_0 and matrix L_0 as

$$L = L_0 + \delta L. \tag{A13}$$

Using that

$$\frac{1}{f(x)} - \frac{1}{f_0} \simeq -\left(\frac{\sigma}{f_0^2}\right)x^2, \tag{A14}$$

we write Eq. (A12) as

$$E_o(x) = e^{-i\frac{\pi}{\lambda}\frac{x^2}{f_0}}\left[1 + \left(e^{\frac{i\pi\sigma}{\lambda f_0^2}x^4} - 1\right)\right]E_i(x), \tag{A15}$$

which allows us to express the action of the aberration operator $\delta L : E_i \to E_o$ as

$$E_o \simeq \left[\exp\left(i\frac{\pi}{\lambda}\frac{\sigma}{f_0^2}x^4\right) - 1\right]\exp\left(-i\frac{\pi}{\lambda}\frac{x^2}{f_0}\right)E_i. \tag{A16}$$

Finally, we will employ the proximity of the SIC to simplify the representation of the round-trip operator in the presence of the aberrations. The full operator W [cf. Eq. (A5)] is given by

$$W = D_1 L D_2 M M D_2 L D_1.$$

Using Eq. (A13), we can expand W as

$$W = W_0 + \delta W, \tag{A17}$$

where we defined the unperturbed round-trip operator as $W_0 = D_1 L_0 D_2 M D_2 L_0 D_1$. The expression of δW reads after simplification and to the first order in $O(\delta L)$:

$$\delta W = D_1(\delta L)L_0^{-1}D_1^{-1}W_0 + W_0 D_1^{-1}L_0^{-1}(\delta L)D_1. \tag{A18}$$

Further, we can simplify the dependence on δL in Eq. (A18) using the exact SIC, which amounts to setting $W_0 = \text{Id}$ in Eq. (A18). Indeed, since δL is already a small quantity, the error incurred in setting $W_0 = \text{Id}$ will be second order. We are left calculating the two contributions of aberrations to the round-trip field evolution. We have $\delta W = F_1 + F_2$ with

$$F_1 = D_1(\delta L)L_0^{-1}D_1^{-1}, \quad F_2 = D_1^{-1}L_0^{-1}(\delta L)D_1. \tag{A19}$$

In both cases, we can express F_j as a double integral involving the HFT that involves the spherical aberration of the lens. We combine the two steps corresponding to $\gamma_{1\to 2} = L_0^{-1}D_1^{-1}$ and $\gamma_{2\to 1} = D_1^{-1}L_0^{-1}$ into a single Fresnel transform. Further, we employ the SIC to find

$$\gamma_{1\to 2} = \begin{pmatrix} 1 & -f\left(1 + \frac{f}{R}\right) \\ \frac{1}{f} & -\frac{f}{R} \end{pmatrix}, \tag{A20}$$

$$\gamma_{2\to 1} = \begin{pmatrix} -\frac{f}{R} & -f\left(\frac{f}{R} + 1\right) \\ \frac{1}{f} & 1 \end{pmatrix}. \tag{A21}$$

As a last approximation, we consider the limit of a long cavity for which the focal length of the mirror is large in comparison with the focal length of the collimator lens. As such, we can define $\varepsilon = f/R \ll 1$. This allows us to approximate the operators γ_j as

$$\gamma_{1\to 2} = \begin{pmatrix} 1 & -f_0 \\ \frac{1}{f_0} & 0 \end{pmatrix} + O(\varepsilon), \tag{A22}$$

$$\gamma_{2\to 1} = \begin{pmatrix} 0 & -f_0 \\ \frac{1}{f_0} & 1 \end{pmatrix} + O(\varepsilon). \tag{A23}$$

Writing the action of F_1 using three integral transforms $F_1 : E_0 \to E_3$ leads to

$$E_1(x) = e^{i\frac{\pi}{\lambda f_0}x^2}\int_{-\infty}^{\infty} E_0(\xi)\sqrt{\frac{i}{\lambda f_0}}\exp\left[-i\frac{\pi}{\lambda f_0}(\xi - x)^2\right]d\xi,$$

$$E_2(x) = \left(e^{i\frac{\pi}{\lambda}\frac{\sigma x^4}{f_0^2}} - 1\right)e^{-i\frac{\pi}{\lambda f_0}x^2}E_1(x),$$

$$E_3(x) = \sqrt{\frac{-i}{\lambda f_0}}\int_{-\infty}^{\infty} E_2(\xi)\exp\left[i\frac{\pi}{\lambda f_0}(\xi - x)^2\right]d\xi. \tag{A24}$$

The action of F_1 can be expressed by the following kernel:

$$E_3 = \int_{-\infty}^{\infty} E_0(z)K_1(x, z)dz, \tag{A25}$$

where the kernel K_1 is defined as

$$K_1(x, z) = \frac{1}{\lambda f_0}e^{-i\frac{\pi}{\lambda f_0}(z-x)(z+x)} \tag{A26}$$

$$\times \int_{-\infty}^{\infty}\left(e^{i\frac{\pi}{\lambda}\frac{\sigma y^4}{f_0^2}} - 1\right)e^{i\frac{2\pi}{\lambda f_0}(z-x)y}dy.$$

For small aberration, we can expand K_1 at first order in σ, which leads to

$$K_1(x, z) \simeq \frac{i\pi\sigma}{\lambda^2 f_0^3}e^{-i\frac{\pi}{\lambda f_0}(z-x)(z+x)}\int_{-\infty}^{\infty} y^4 e^{i\frac{2\pi}{\lambda f_0}(z-x)y}dy.$$

Using $t = 2\pi y/(\lambda f_0)$, we find

$$K_1(x, z) = i\frac{\sigma f_0^2}{2k^3}e^{-i\frac{\pi}{\lambda f_0}(z-x)(z+x)}\delta^{(4)}(z - x), \tag{A27}$$

where we used the fact that

$$\int_{-\infty}^{\infty} t^n e^{i\omega t}dt = 2\pi(-i)^n\delta^{(n)}(\omega). \tag{A28}$$

Here, we defined $\delta^{(n)}$ as the nth derivative of the Dirac delta which associates with the local value of the nth derivative of a function. Since $\delta^{(n)}$ is a well-localized function, we can set $z = x$ and obtain

$$K_1(x, z) = i\frac{\sigma f_0^2}{2k^3}\delta^{(4)}(z - x). \tag{A29}$$

Performing the convolution with $\delta^{(n)}$ is identical to taking the fourth derivative in direct space which yields the fourth derivative contribution. The action of F_1 to first order is

$$F_1 : E_0 \to E_3,$$

$$E_3(x) = i\frac{\sigma f_0^2}{2k^3}\partial_x^4 E_0(x). \tag{A30}$$

The action of F_2 can be found in a similar fashion using three integral transforms $F_2 : E_0 \to E_3$ and reads

$$E_1(x) = \int_{-\infty}^{\infty} E_0(\xi, 0)\sqrt{\frac{-i}{\lambda f_0}}\exp\left[i\frac{\pi}{\lambda f_0}(\xi - x)^2\right]d\xi,$$

$$E_2(x) = \left(e^{i\frac{\pi}{\lambda}\frac{\sigma x^4}{f_0^2}} - 1\right)e^{-i\frac{\pi}{\lambda f_0}x^2}E_1(x),$$

$$E_3(x) = \sqrt{\frac{i}{\lambda f_0}} \int_{-\infty}^{\infty} E_2(\xi)$$
$$\times \exp\left[-i\frac{\pi}{\lambda f_0}(-2x\xi + x^2)\right]d\xi. \qquad (A31)$$

Similarly, the action of F_2 can be expressed as a integral

$$E_3 = \int_{-\infty}^{\infty} E_0(z,0)K_2(x,z)dz, \qquad (A32)$$

where we defined the kernel K_2 as

$$K_2(x,z) = \frac{1}{\lambda f_0} e^{i\frac{\pi}{\lambda f_0}(z-x)(z+x)}$$
$$\times \int_{-\infty}^{\infty} \left(e^{i\frac{\pi}{\lambda}\frac{\sigma y^4}{f_0^2}} - 1\right) \exp\left[i\frac{2\pi}{\lambda f_0}y(x-z)\right]dy. \qquad (A33)$$

Expanding analogously the aberration contribution to first order in σ and using Eq. (A28), we obtain the desired kernel

$$K_2(x,z) = i\frac{\sigma f_0^2}{2k^3}\delta^{(4)}(z-x). \qquad (A34)$$

We conclude that, to the first order in σ, the action of F_2 is identical to that of F_1:

$$F_2 : E_0 \to E_3,$$
$$E_3(x) = i\frac{\sigma f_0^2}{2k^3}\partial_x^4 E_0(x). \qquad (A35)$$

In summary, the total effect due to spherical aberration close to self-imaging in the one-dimensional case reads

$$E_3(x) = i\frac{\sigma f_0^2}{k^3}\partial_x^4 E_0(x). \qquad (A36)$$

The generalization of these calculations to two-dimensions proceeds without difficulties and yields

$$E_3(r_\perp) = i\frac{\sigma f_0^2}{k^3}\nabla_\perp^4 E_0(r_\perp). \qquad (A37)$$

[1] L. Lugiato, Transverse nonlinear optics: Introduction and review, Chaos Solitons Fractals **4**, 1251 (1994).

[2] J. Lega, J. Moloney, and A. Newell, Swift-Hohenberg equation for lasers, Phys. Rev. Lett. **73**, 2978 (1994).

[3] G. Huyet, M. C. Martinoni, J. R. Tredicce, and S. Rica, Spatiotemporal dynamics of lasers with a large Fresnel number, Phys. Rev. Lett. **75**, 4027 (1995).

[4] K. Staliūnas, G. Šlekys, and C. O. Weiss, Nonlinear pattern formation in active optical systems: Shocks, domains of tilted waves, and cross-roll patterns, Phys. Rev. Lett. **79**, 2658 (1997).

[5] V. B. Taranenko, K. Staliunas, and C. O. Weiss, Pattern formation and localized structures in degenerate optical parametric mixing, Phys. Rev. Lett. **81**, 2236 (1998).

[6] F. Arecchi, S. Boccaletti, and P. Ramazza, Pattern formation and competition in nonlinear optics, Phys. Rep. **318**, 1 (1999).

[7] S. Barland, J. R. Tredicce, M. Brambilla, L. A. Lugiato, S. Balle, M. Giudici, T. Maggipinto, L. Spinelli, G. Tissoni, T. Knödl, M. Miller, and R. Jäger, Cavity solitons as pixels in semiconductor microcavities, Nature (London) **419**, 699 (2002).

[8] T. Ackemann, W. J. Firth, and G. Oppo, Fundamentals and applications of spatial dissipative solitons in photonic devices, in *Advances in Atomic Molecular and Optical Physics*, edited by P. R. B. E. Arimondo and C. C. Lin (Elsevier Inc., 2009), Vol. 57, Chap. 6, pp. 323–421.

[9] P. Genevet, S. Barland, M. Giudici, and J. R. Tredicce, Bistable and addressable localized vortices in semiconductor lasers, Phys. Rev. Lett. **104**, 223902 (2010).

[10] J. Javaloyes, Cavity light bullets in passively mode-locked semiconductor lasers, Phys. Rev. Lett. **116**, 043901 (2016).

[11] S. S. Gopalakrishnan, K. Panajotov, M. Taki, and M. Tlidi, Dissipative light bullets in Kerr cavities: Multistability, clustering, and rogue waves, Phys. Rev. Lett. **126**, 153902 (2021).

[12] L. G. Wright, P. Sidorenko, H. Pourbeyram, Z. M. Ziegler, A. Isichenko, B. A. Malomed, C. R. Menyuk, D. N. Christodoulides, and F. W. Wise, Mechanisms of spatiotemporal mode-locking, Nat. Phys. **16**, 565 (2020).

[13] Y. Ding, X. Xiao, K. Liu, S. Fan, X. Zhang, and C. Yang, Spatiotemporal mode-locking in lasers with large modal dispersion, Phys. Rev. Lett. **126**, 093901 (2021).

[14] L. G. Wright, W. H. Renninger, D. N. Christodoulides, and F. W. Wise, Nonlinear multimode photonics: Nonlinear optics with many degrees of freedom, Optica **9**, 824 (2022).

[15] F. Leo, S. Coen, P. Kockaert, S.-P. Gorza, P. Emplit, and M. Haelterman, Temporal cavity solitons in one-dimensional Kerr media as bits in an all-optical buffer, Nat. Photonics **4**, 471 (2010).

[16] T. Herr, V. Brasch, J. D. Jost, C. Y. Wang, N. M. Kondratiev, M. L. Gorodetsky, and T. J. Kippenberg, Temporal solitons in optical microresonators, Nat. Photonics **8**, 145 (2014).

[17] M. Marconi, J. Javaloyes, S. Balle, and M. Giudici, How lasing localized structures evolve out of passive mode locking, Phys. Rev. Lett. **112**, 223901 (2014).

[18] M. Tlidi and L. Gelens, High-order dispersion stabilizes dark dissipative solitons in all-fiber cavities, Opt. Lett. **35**, 306 (2010).

[19] P. Parra-Rivas, D. Gomila, F. Leo, S. Coen, and L. Gelens, Third-order chromatic dispersion stabilizes Kerr frequency combs, Opt. Lett. **39**, 2971 (2014).

[20] K. K. K. Tam, T. J. Alexander, A. Blanco-Redondo, and C. M. de Sterke, Generalized dispersion Kerr solitons, Phys. Rev. A **101**, 043822 (2020).

[21] F. Leo, A. Mussot, P. Kockaert, P. Emplit, M. Haelterman, and M. Taki, Nonlinear symmetry breaking induced by third-order dispersion in optical fiber cavities, Phys. Rev. Lett. **110**, 104103 (2013).

[22] M. Tlidi, A. Mussot, E. Louvergneaux, G. Kozyreff, A. G. Vladimirov, and M. Taki, Control and removal of modulational instabilities in low-dispersion photonic crystal fiber cavities, Opt. Lett. **32**, 662 (2007).

[23] M. Droques, A. Kudlinski, G. Bouwmans, G. Martinelli, A. Mussot, A. Armaroli, and F. Biancalana, Fourth-order dispersion mediated modulation instability in dispersion oscillating fibers, Opt. Lett. **38**, 3464 (2013).

[24] A. Blanco-Redondo, C. M. de Sterke, J. E. Sipe, T. F. Krauss, B. J. Eggleton, and C. Husko, Pure-quartic solitons, Nat. Commun. **7**, 10427 (2016).

[25] C. M. de Sterke, A. F. J. Runge, D. D. Hudson, and A. Blanco-Redondo, Pure-quartic solitons and their generalizations—theory and experiments, APL Photonics **6**, 091101 (2021).

[26] M. Karlsson and A. Höök, Soliton-like pulses governed by fourth order dispersion in optical fibers, Opt. Commun. **104**, 303 (1994).

[27] J. A. Arnaud, Degenerate optical cavities, Appl. Opt. **8**, 189 (1969).

[28] A. E. Siegman, *Lasers* (University Science Books, Mill Valley, CA, 1986).

[29] X. Hachair, S. Barbay, T. Elsass, I. Sagnes, and R. Kuszelewicz, Transverse spatial structure of a high Fresnel number vertical external cavity surface emitting laser, Opt. Express **16**, 9519 (2008).

[30] I. A. Litvin, N. A. Khilo, A. Forbes, and V. N. Belyi, Intra–cavity generation of Bessel-like beams with longitudinally dependent cone angles, Opt. Express **18**, 4701 (2010).

[31] A. Bartolo, N. Vigne, M. Marconi, G. Beaudoin, K. Pantzas, I. Sagnes, G. Huyet, F. Maucher, S. V. Gurevich, J. Javaloyes, A. Garnache, and M. Giudici, Temporal localized Turing patterns in mode-locked semiconductor lasers, Optica **9**, 1386 (2022).

[32] N. Vigne, 3D structured coherent light state emitted by a self imaging laser cavity based on semiconductor VECSEL technology, Ph.D. thesis, Université de Montpellier, 2022.

[33] S. Knitter, C. Liu, B. Redding, M. K. Khokha, M. A. Choma, and H. Cao, Coherence switching of a degenerate VECSEL for multimodality imaging, Optica **3**, 403 (2016).

[34] S. Mahler, Y. Eliezer, H. Yılmaz, A. A. Friesem, N. Davidson, and H. Cao, Fast laser speckle suppression with an intracavity diffuser, Nanophotonics **10**, 129 (2021).

[35] J. Pupeikis, B. Willenberg, S. L. Camenzind, A. Benayad, P. Camy, C. R. Phillips, and U. Keller, Spatially multiplexed single-cavity dual-comb laser, Optica **9**, 713 (2022).

[36] Y. Eliezer, S. Mahler, A. A. Friesem, H. Cao, and N. Davidson, Controlling nonlinear interaction in a many-mode laser by tuning disorder, Phys. Rev. Lett. **128**, 143901 (2022).

[37] A. Bartolo, N. Vigne, M. Marconi, G. Beaudoin, L. L. Gratiet, K. Pantzas, I. Sagnes, A. Garnache, and M. Giudici, Spatiotemporally reconfigurable light in degenerate laser cavities, Photonics Res. **11**, 1751 (2023).

[38] H. Cao, R. Chriki, S. Bittner, A. A. Friesem, and N. Davidson, Complex lasers with controllable coherence, Nat. Rev. Phys. **1**, 156 (2019).

[39] J. Turunen, A. Vasara, and A. T. Friberg, Propagation invariance and self-imaging in variable-coherence optics, J. Opt. Soc. Am. A **8**, 282 (1991).

[40] K. Kim, S. Bittner, Y. Jin, Y. Zeng, S. Guazzotti, O. Hess, Q. J. Wang, and H. Cao, Sensitive control of broad-area semiconductor lasers by cavity shape, APL Photonics **7**, 056106 (2022).

[41] M. Piccardo, M. de Oliveira, A. Toma, V. Aglieri, A. Forbes, and A. Ambrosio, Vortex laser arrays with topological charge control and self-healing of defects, Nat. Photonics **16**, 359 (2022).

[42] Y. Slobodkin, G. Weinberg, H. Hörner, K. Pichler, S. Rotter, and O. Katz, Massively degenerate coherent perfect absorber for arbitrary wavefronts, Science **377**, 995 (2022).

[43] M. Yang, H.-Q. Zhang, Y.-W. Liao, Z.-H. Liu, Z.-W. Zhou, X.-X. Zhou, J.-S. Xu, Y.-J. Han, C.-F. Li, and G.-C. Guo, Topological band structure via twisted photons in a degenerate cavity, Nat. Commun. **13**, 2040 (2022).

[44] R. Chriki, G. Barach, C. Tradosnky, S. Smartsev, V. Pal, A. A. Friesem, and N. Davidson, Rapid and efficient formation of propagation invariant shaped laser beams, Opt. Express **26**, 4431 (2018).

[45] L. W. Clark, N. Schine, C. Baum, N. Jia, and J. Simon, Observation of Laughlin states made of light, Nature (London) **582**, 41 (2020).

[46] M. Jaffe, L. Palm, C. Baum, L. Taneja, and J. Simon, Aberrated optical cavities, Phys. Rev. A **104**, 013524 (2021).

[47] Y. A. Vlasov, M. O'Boyle, H. F. Hamann, and S. J. McNab, Active control of slow light on a chip with photonic crystal waveguides, Nature (London) **438**, 65 (2005).

[48] L. H. Frandsen, A. V. Lavrinenko, J. Fage-Pedersen, and P. I. Borel, Photonic crystal waveguides with semi-slow light and tailored dispersion properties, Opt. Express **14**, 9444 (2006).

[49] K. Staliunas, C. Serrat, R. Herrero, C. Cojocaru, and J. Trull, Subdiffractive light pulses in photonic crystals, Phys. Rev. E **74**, 016605 (2006).

[50] A. Khanolkar, Y. Zang, and A. Chong, Complex Swift-Hohenberg equation dissipative soliton fiber laser, Photonics Res. **9**, 1033 (2021).

[51] M. Tlidi, P. Mandel, and R. Lefever, Localized structures and localized patterns in optical bistability, Phys. Rev. Lett. **73**, 640 (1994).

[52] J.-F. Mercier and J. V. Moloney, Derivation of semiconductor laser mean-field and Swift-Hohenberg equations, Phys. Rev. E **66**, 036221 (2002).

[53] L. Gelens, G. Van der Sande, P. Tassin, M. Tlidi, P. Kockaert, D. Gomila, I. Veretennicoff, and J. Danckaert, Impact of nonlocal interactions in dissipative systems: Towards minimal-sized localized structures, Phys. Rev. A **75**, 063812 (2007).

[54] P. Kockaert, P. Tassin, I. Veretennicoff, G. V. der Sande, and M. Tlidi, Beyond the zero-diffraction regime in optical cavities with a left-handed material, J. Opt. Soc. Am. B **26**, B148 (2009).

[55] L. Gelens, D. Gomila, G. Van der Sande, J. Danckaert, P. Colet, and M. A. Matías, Dynamical instabilities of dissipative solitons in nonlinear optical cavities with nonlocal materials, Phys. Rev. A **77**, 033841 (2008).

[56] M. Tlidi, P. Kockaert, and L. Gelens, Dark localized structures in a cavity filled with a left-handed material, Phys. Rev. A **84**, 013807 (2011).

[57] O. Firstenberg, P. London, M. Shuker, A. Ron, and N. Davidson, Elimination, reversal and directional bias of optical diffraction, Nat. Phys. **5**, 665 (2009).

[58] F. Gustave, N. Radwell, C. McIntyre, J. P. Toomey, D. M. Kane, S. Barland, W. J. Firth, G.-L. Oppo, and T. Ackemann, Observation of mode-locked spatial laser solitons, Phys. Rev. Lett. **118**, 044102 (2017).

[59] S. V. Gurevich and J. Javaloyes, Spatial instabilities of light bullets in passively-mode-locked lasers, Phys. Rev. A **96**, 023821 (2017).

[60] A. Ashkin, J. M. Dziedzic, J. E. Bjorkholm, and S. Chu, Observation of a single-beam gradient force optical trap for dielectric particles, Opt. Lett. **11**, 288 (1986).

[61] M. Woerdemann, C. Alpmann, M. Esseling, and C. Denz, Advanced optical trapping by complex beam shaping, Laser Photonics Rev. **7**, 839 (2013).

[62] C. J. Bustamante, Y. R. Chemla, S. Liu, and M. D. Wang, Optical tweezers in single-molecule biophysics, Nat. Rev. Methods Primers **1**, 25 (2021).

[63] K. Staliunas, R. Herrero, and G. de Valcárcel, Sub-diffractive band-edge solitons in Bose-Einstein condensates in periodic potentials, Phys. Rev. E **73**, 065603(R) (2006).

[64] M. R. Andrews, C. G. Townsend, H.-J. Miesner, D. S. Durfee, D. M. Kurn, and W. Ketterle, Observation of interference between two Bose condensates, Science **275**, 637 (1997).

[65] Y. Shin, M. Saba, T. A. Pasquini, W. Ketterle, D. E. Pritchard, and A. E. Leanhardt, Atom interferometry with Bose-Einstein condensates in a double-well potential, Phys. Rev. Lett. **92**, 050405 (2004).

[66] P. Camelin, J. Javaloyes, M. Marconi, and M. Giudici, Electrical addressing and temporal tweezing of localized pulses in passively-mode-locked semiconductor lasers, Phys. Rev. A **94**, 063854 (2016).

[67] C. Schelte, D. Hessel, J. Javaloyes, and S. V. Gurevich, Dispersive instabilities in passively mode-locked integrated external-cavity surface-emitting lasers, Phys. Rev. Appl. **13**, 054050 (2020).

[68] J. Hausen, K. Lüdge, S. V. Gurevich, and J. Javaloyes, How carrier memory enters the Haus master equation of mode-locking, Opt. Lett. **45**, 6210 (2020).

[69] C. Palma and V. Bagini, Extension of the Fresnel transform to ABCD systems, J. Opt. Soc. Am. A **14**, 1774 (1997).

[70] G. New, Pulse evolution in mode-locked quasi-continuous lasers, IEEE J. Quantum Electron. **10**, 115 (1974).

[71] N. N. Rosanov and G. V. Khodova, Diffractive autosolitons in nonlinear interferometers, J. Opt. Soc. Am. B **7**, 1057 (1990).

[72] A. G. Vladimirov, S. V. Fedorov, N. A. Kaliteevskii, G. V. Khodova, and N. N. Rosanov, Numerical investigation of laser localized structures, J. Opt. B: Quantum Semiclassical Opt. **1**, 101 (1999).

[73] H. Uecker, D. Wetzel, and J. D. M. Rademacher, pde2path: A Matlab package for continuation and bifurcation in 2D elliptic systems, NMTMA **7**, 58 (2019).

[74] A. Bartolo, N. Vigne, M. Marconi, G. Beaudoin, K. Pantzas, I. Sagnes, A. Garnache, and M. Giudici, Time localized tilted beams in nearly-degenerate laser cavities, arXiv:2401.11886.

[75] M. A. Fuentes, M. N. Kuperman, and V. M. Kenkre, Nonlocal interaction effects on pattern formation in population dynamics, Phys. Rev. Lett. **91**, 158104 (2003).

[76] F. Maucher, T. Pohl, S. Skupin, and W. Krolikowski, Self-organization of light in optical media with competing nonlinearities, Phys. Rev. Lett. **116**, 163902 (2016).

[77] J. Javaloyes, M. Marconi, and M. Giudici, Nonlocality induces chains of nested dissipative solitons, Phys. Rev. Lett. **119**, 033904 (2017).